Residual motion artifact removal enables dynamic μMRI of a behaving *Pachnoda marginata*

Ajmal Chenakkara [a], Mazin Jouda [a], Ulrike Wallrabe [b], Jan G. Korvink [a] [iD],*

[a] *Institute of Microstructure Technology (IMT), Karlsruhe Institute of Technology (KIT), Germany*
[b] *Institute of Microsystem Technology (IMTEK), University of Freiburg, Germany*

ARTICLE INFO

ABSTRACT

Microscopic magnetic resonance imaging, also referred to as μMRI, is a non-invasive imaging modality ideal for studying small live model organisms. However, μMRI raw data acquisition is inherently sequential and slow in comparison to the biomechanics timescale of the behaving organism, leading to motion artifacts upon image reconstruction. Recently, we have developed an integrated spherical treadmill with a prospectively triggered k-space acquisition technique to provide position consistency for studying live, behaving insect using μMRI. Despite this advancement, behaving insects on the treadmill still exhibited motion artifacts due to tethered locomotion being coupled with internal organ dynamics. Here, we are addressing the large-scale non-rigid nature of the abdominal motion of the behaving insect by developing a fully retrospective gating strategy using the motion information obtained from an in-situ computer vision system. Residual motion artifacts persisting after gating are effectively managed through a deep learning technique. We trained a U-Net-based deep convolutional neural network using pairs of simulated motion-corrupted and motion-free images as a supervised image-to-image translation problem. Our results demonstrate that combining retrospective gated μMRI reconstruction with a deep learning residual motion compensation technique can significantly reduce the motional artifacts, thereby paving the way for the non-invasive dynamic imaging studies of behaving organisms with 117 μm in-plane resolution.

1. Introduction

Studying live, naturally behaving model organisms is fundamental to advancements in various fields of zoology. Magnetic resonance imaging is a non-invasive modality which is ideal for probing a live biological entity. The low sensitivity and inherently sequential acquisition of MRI raw data (k-space) makes it underutilized in terms of methodological developments for behaving model organisms, especially in the magnetic resonance microscopy domain (MRM). The typical physiological and ethological motion time scale of a behaving model organism often falls within a range that can significantly degrade the quality of MR image reconstruction. Many MRI reconstruction methods assume a stationary subject. Therefore, movements during the sequential k-space acquisition result in a model mismatch between the MR coordinate system and the subject's co-moving coordinate system, leading to motion artifacts. The ubiquitous problem of motion in MRI, its effects, characterization, and mitigation strategies have a large body of literature since the inception of clinical MRI, and have been reviewed elsewhere [1,2].

Recently, we demonstrated that an integrated spherical treadmill technique can provide spatial consistency for MR acquisition, with minimal restriction to movement for the tethered behaving organism [3]. This technique essentially constrains the motion within the MRI field of view (FOV), or the selected imaging slice, rendering motion artifacts manageable using a prospectively triggered MRI k-space acquisition strategy. The overall motion model of a behaving insect on a treadmill can be characterized as a combination of rigid and non-rigid body motion. While prospective triggered k-space acquisition has proven to be an effective method for mitigating the impact of non-rigid abdominal motion in the behaving *Pachnoda marginata* model organism, some residual motion artifacts from flexible body regions may still persist, adversely affecting MRI reconstruction quality [3]. In the present study, we introduce an additional, fully retrospective technique for motion-corrected MRI of the active insect, combining retrospective gating to address large-scale non-rigid motion, and a deep learning method for residual motion artifact correction. An optical flow computer vision system has been integrated with the high-field magnet, which can estimate the body motion parameters retrospectively [3]. The MRI k-space
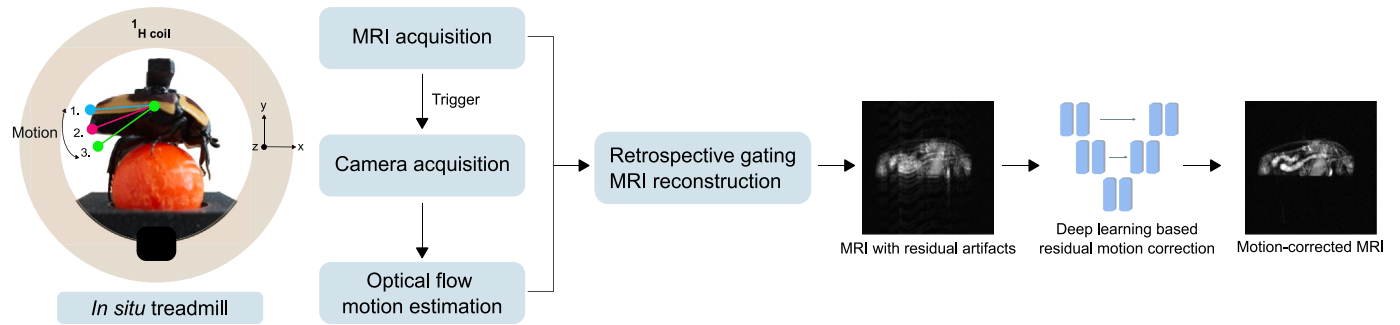
Fig. 1. Schematic diagram illustrating the two-stage MRI motion compensation process for a behaving *Pachnoda marginata* on a treadmill: initial compensation via retrospective gating, and subsequent deep learning residual motion correction.

acquisition is synchronized with the optical imaging and employs a continuous acquisition scheme, with MRI frame repetitions specifically aligned to match the physiological timescale of the insect's behavior. Motion-compensated MR image frames can be retrospectively recovered by aligning the insect motion states with the corresponding phase encoding steps, analogous to the retrospective cardiac and respiratory gating techniques used in clinical MRI [4–6].

In general, any prospective or retrospective motion correction strategy that employs external devices or MR-based internal measurements for motion estimation will inevitably introduce some degree of uncertainty, potentially leading to residual artifacts in image reconstruction [7,8]. Modeling the residual motion artifacts is highly challenging, due to the complex nature of ensemble effects contributing to them, to render this a highly ill-posed problem, especially for the case of insect locomotion. However, residual motion artifacts are less severe, mostly localized, and can be approximated with a linear translational and rotational motion model. Data-driven techniques are ideal for addressing this type of problem and have been quite successful in clinical MRI motion correction research [9]. Deep learning MRI motion correction is a rapidly evolving field of research, with extensive reviews available elsewhere [9–11]. Although numerous learning-based methods have been explored for MRI motion correction, supervised image-to-image translation approaches leveraging variations of deep convolutional neural networks in the image magnitude space dominate due to their simplicity, effectiveness, and broad applicability in addressing the motion artifacts [12,13]. This approach necessitates a large dataset of paired images, containing instances with and without motion artifacts, which is often challenging and expensive to obtain. Consequently, most motion correction strategies depend on simulated datasets, often derived from large public clinical MRI repositories. In-plane motion artifacts in MRI are typically simulated using k-space or image-space techniques by modeling rigid body translation and rotation as the primary sources of these artifacts [2,14]. For the case of insect locomotion in MRI, obtaining large ground truth motion-free MRI dataset is still expensive and laborious. Transfer learning can be an effective approach in mitigating the data scarcity problem when training a deep neural networks [15,16]. The model can be pre-trained with a source domain of motion-corrupted dataset simulated from a large publicly available brain MRI dataset [17], enabling the model to learn generalizable features associated with the motion artifacts. By fine-tuning this pre-trained model on a small target domain dataset of insect MRI with simulated motion artifacts, the network adapts to the specific structural and textural characteristics of insect anatomy while retaining useful feature representations from the source domain (see Fig. 1).

2. Materials and methods

2.1. Treadmill MRI setup

MRI experiments were carried out on a 15.2 T (Bruker Biospin - Ettlingen, Germany) high-field magnet with a 35 mm inner diameter

quadrature ^1H bird cage RF coil tuned to 650 MHz. In our previous study, we introduced a spherical treadmill MRI platform with an integrated computer vision system for studying live behaving insect using high-field MRI [3]. The setup featured a 3D-printed structure designed to securely tether the live insect, coupled with an air-cushioned spherical ball that enables minimally restricted locomotion. This assembly was seamlessly integrated with the RF volume coil, as illustrated in Fig. 2(a),(b)&(c). Detailed information on the design and working of the treadmill MRI can be found here [3].

2.2. In situ MR compatible computer vision system and motion tracking

The real-time motion and physiological response of the insect inside the high-field magnet were monitored using an integrated computer vision setup [3]. The setup included a modified commercial webcam (Microsoft LifeCam HD-3000, maximum FPS of 30 Hz, 1280 × 720 pixel resolution) with a white LED for illumination, mounted with 3D-printed parts for MR compatibility. The imaging system was aligned horizontally with the RF volume coil and connected to the acquisition computer via a 20-meter USB repeater cable. The system's placement and MR compatibility was validated, and the details of its impact on MRI experiments are discussed here [3].

The in-situ camera image capture was synchronized with the MRI acquisition using an Arduino-based triggering setup, as represented in Fig. 3(a). The MR imaging pulse sequence sent a TTL signal to the camera via an Arduino to start and stop the camera acquisition. A Python program managed camera acquisition by reading serial input from the Arduino triggered by the TTL signal. After the MRI acquisition, the saved video file was used for motion estimation as a post processing step. We utilized a sparse optical flow algorithm to precisely track the motion of a predefined keypoint, specifically targeting the posterior region of the insect's abdomen as shown in Fig. 2(g)&(k). The methodology, theory, and the uncertainty in the motion estimation of the developed optical flow algorithm can be found here [3]. A sample video file (Video 1) showing the single point tracking is provided with the supplementary materials.

2.3. Retrospective gating for initial motion correction

The motion model of the in situ behaving insect locomotion on the treadmill is a combination of head motion, abdominal motion, internal organ motion, and leg motion. Each of these can be described as a combination of rigid and non-rigid movements, due to both mechanism kinematics of the exoskeleton, and deformation of the soft tissue due to muscle and organ movement. In this study, we focused on the semi-periodic, non-rigid motion of the insect's abdomen. We approximated its large-scale movement as a multi-rigid system with two primary components: a static horizontal body segment, primarily consisting of the thorax, and the abdomen, represented as three distinct motion states in Fig. 3(b).
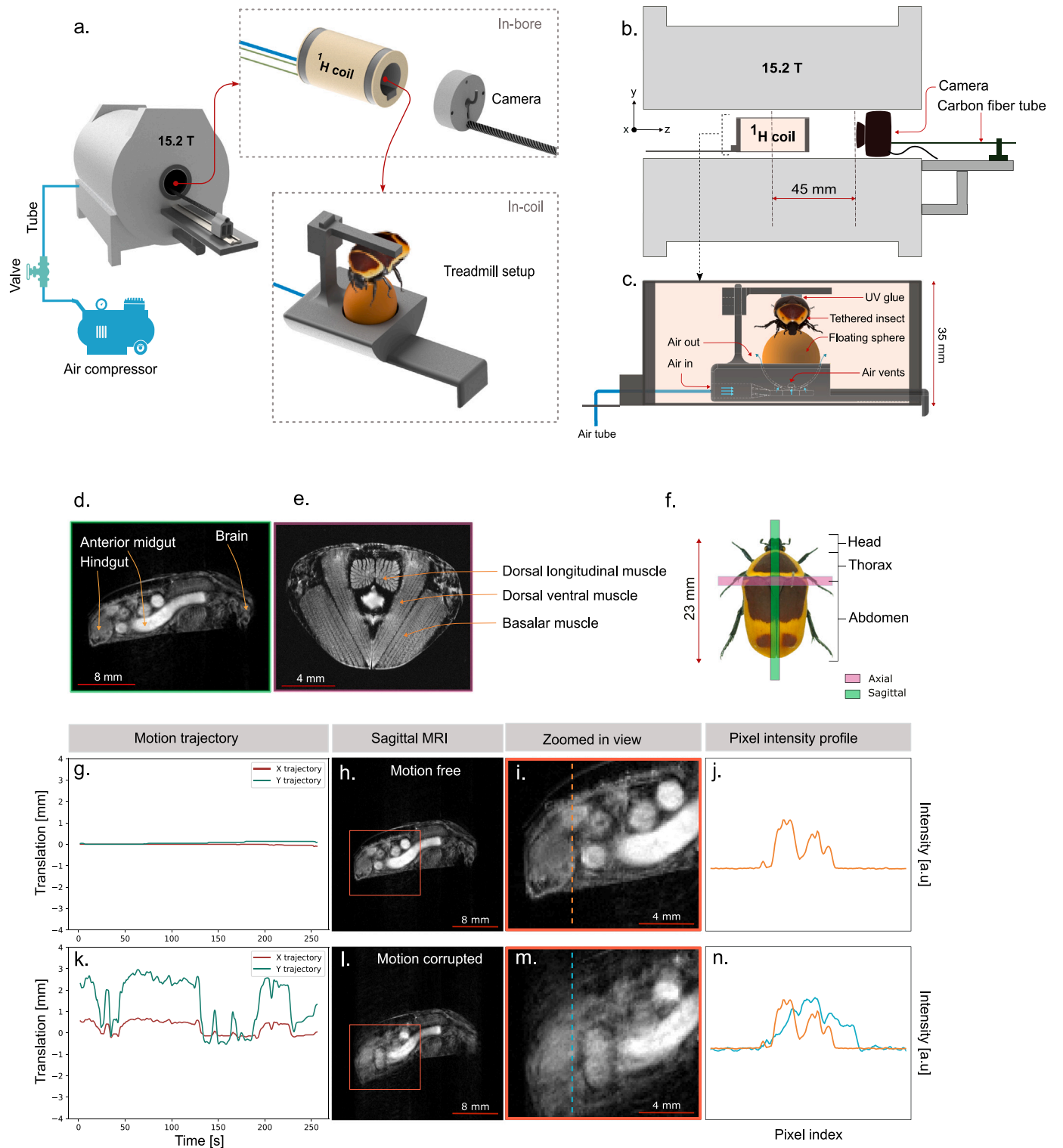
Fig. 2. *In situ* treadmill setup for behaving insect MRI. **(a)** Treadmill setup with 15.2 T magnet. **(b)** Treadmill setup *in situ* RF volume coil. **(c)** Illustration of tethered behaving insect on treadmill. **(d)** Sagittal anatomic MRI of inactive insect showing the alimentary canal. **(e)** Axial MRI of the inactive insect showing the thorax region. **(f)** Insect MRI slice position reference. **(g)** Motion trajectory of the abdomen of the inactive insect. **(h)** Sagittal MRI of the inactive insect as ground truth. **(i)** Zoomed-in view showing the insect abdomen without motion artifacts. **(j)** Corresponding pixel intensity profile. **(k)** Motion trajectory of the abdomen of the behaving insect. **(l)** Sagittal MRI of the same slice of the behaving insect showing motion artifacts. **(m)** Zoomed-in view of the same. **(n)** Corresponding pixel intensity profile illustrating the distortion caused by motion. Results adapted from Chenakkara et al. [3].

We developed a retrospective gating strategy for this multi-rigid motion compensation. The MRI experiment involved continuous acquisition of 2D k-space data from a selected sagittal slice over multiple frame repetitions. We employed the fast spin-echo-based MRI sequence

RARE (Rapid Acquisition with Relaxation Enhancement) available in the Paravision 360 v3.3 (Bruker BioSpin - Ettlingen, Germany) to image a sagittal slice of the insect (position reference in Fig. 5(b)). The MR imaging parameters included a repetition time of 250 ms, an

echo time of $5\,\mathrm{ms}$, and an image matrix of 256×256 pixels with a field of view (FOV) of $30\,\mathrm{mm} \times 30\,\mathrm{mm}$. The sequence was configured without signal averaging, with a RARE factor of one, a slice thickness of $1\,\mathrm{mm}$, and 50 repetitions to acquire dynamic MRI frames. This setup resulted in a total acquisition time of $53\,\mathrm{min}\,20\,\mathrm{s}$ and an in-plane image resolution of $117\,\mu\mathrm{m} \times 117\,\mu\mathrm{m}$. The total number of phase encoding or k-space lines was a multiple of MRI frame repetitions. Optical imaging acquisition was synchronized with the MRI acquisition. The 2D motion trajectory of the keypoint was extracted using the optical flow technique [3]. The insect abdominal pose was discretized into position states via grid-based clustering of the motion trajectory, with cluster centroids defining the states. Fig. 6(a) presents the motion trajectory of the annotated keypoint (posterior part of the insect abdomen) during k-space acquisition, with color-coding indicating the spatial clusters identified through grid-based categorization. We defined 14 clusters using a 4×4 equally spaced 2D spatial grid, excluding any grid cells that did not contain data points. Fig. 6(b) displays a 2D X-Y plot of the same trajectory, where the cluster centroids defines the position states for the gated MRI reconstruction. The standard deviation of points within each cluster, shown in Fig. 6(c), served as a metric for the precision of each position state estimation. Phase encoding steps were then correlated with the insect abdominal pose position states during MRI acquisition, to generate individual k-space matrices for motion-compensated image reconstruction. Multiple k-space frames of the same position state were averaged for better SNR, while gaps in k-space were filled using linear interpolation. Fig. 3 shows an overall schematic of the process, where Fig. 3(a) represents the *in situ* MR compatible computer vision system, Fig. 3(b) shows the *in situ* treadmill setup, Fig. 3(c) illustrates the motion trajectory of the selected keypoint calculated by the optical flow algorithm, and Fig. 3(d) represents the sorted MRI k-space frames corresponding to the discrete position states, which upon reconstruction gives motion compensated images. The overall pipeline is presented in Algorithm 1.

Algorithm 1: Retrospective Gating

Input :

- $\mathbf{K}(k_x, k_y, n)$: 3D k-space (frequency encoding $\times$ phase encoding $\times$ frames).
- $\mathbf{S}(n)$: Motion signal - sparse optical flow motion trajectory of keypoint.

Output: $\{\mathbf{I}_m(x, y)\}_{m=1}^M$: Motion-resolved MRI frames.

1 **I. Bin frames by motion state**
2 Cluster motion signal $\mathbf{S}(n)$ into M states $\{m_1, \ldots, m_M\}$ using grid-based clustering.

3 **II. Assign frames to motion bins**
4 **foreach** *frame n* **do**
5   **Assign** $\mathbf{K}(:, :, n)$ to bin m where $\mathbf{S}(n) \in m$.

6 **III. Reconstruct motion-resolved k-space**
7 **foreach** *motion bin m* **do**
8   **Reconstruct** $\mathbf{K}_m(k_x, k_y) = \mathrm{mean}\{\mathbf{K}(k_x, k_y, n) \mid n \in m\}$.
9   **if** $\mathbf{K}_m$ *has missing* k_y *lines* **then**
10   **Interpolate** using:
11   - Linear interpolation.

12 **IV. Generate motion-resolved images**
13 **foreach** $\mathbf{K}_m$ **do**
14     $\mathbf{I}_m(x, y) = \mathrm{FFT}^{-1}(\mathbf{K}_m(k_x, k_y))$.

2.4. Deep learning for residual motion correction

2.4.1. Datasets

We used two ground truth motion-free datasets for simulating the motion-corrupted images. For the first dataset, we used a publicly
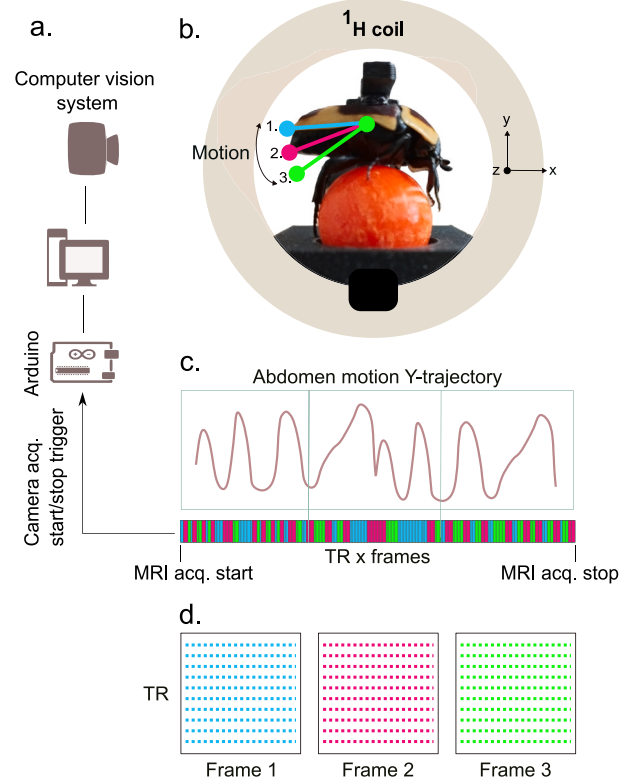

Fig. 3. Schematic representation of the *in-situ* treadmill setup with an MR compatible computer vision system for motion estimation, enabling retrospective gating for motion compensated MRI. **(a)** Computer vision system schematic. **(b)** *In-situ* treadmill setup. **(c)** Motion trajectory of the selected keypoint, with the phase encoding index of the MRI frames. **(d)** Phase encode reordering for position consistent MRI reconstruction.

available T1-weighted adult human brain MRI dataset [17], for which the raw data was originally obtained using a 12-channel imaging coil, with the coil sensitivity maps normalized to create a single complex-valued image set with matrix size of 256×256. The second dataset, which was experimentally acquired, consisted of sagittal MRI slices of inactive insects (see Fig. 2(d) for reference). All the insect imaging experiments were carried out on a $15.2\,\mathrm{T}$ magnet (Bruker Biospin - Ettlingen, Germany) with a $35\,\mathrm{mm}$ inner diameter quadrature ^1H bird cage RF coil tuned to $650\,\mathrm{MHz}$. We used the RARE sequence for the imaging experiments. The imaging parameters included a repetition time (TR) of $500\,\mathrm{ms}$, echo time of $5\,\mathrm{ms}$, and image size of 256×256 pixels with a FOV of $30\,\mathrm{mm}\ x\ 30\,\mathrm{mm}$, resulting in an in-plane spatial resolution of $117\,\mu\mathrm{m} \times 117\,\mu\mathrm{m}$, a slice thickness of $1\,\mathrm{mm}$, and no signal averages. A linear scaling factor of 1.2 was applied to the intensity of all insect MR magnitude images for visualization purposes, unless stated otherwise. Insect MRI anatomical reference images highlighting major anatomical structures are presented in Fig. 2(d)&(e), with the imaging parameters detailed in the supplementary information. While the same insect species (*Pachnoda marginata*) having similar external morphological characteristics was used across multiple experiments in the present study, subtle variations in internal anatomical appearance may occur between individual specimens due to differences in physiological characteristics and variations in MRI acquisition parameters. This contributes to a more diverse and robust dataset for the deep learning model training.

2.4.2. Motion artifact simulation

Supervised training of deep neural networks for MRI motion correction typically requires a substantial dataset of motion-corrupted and
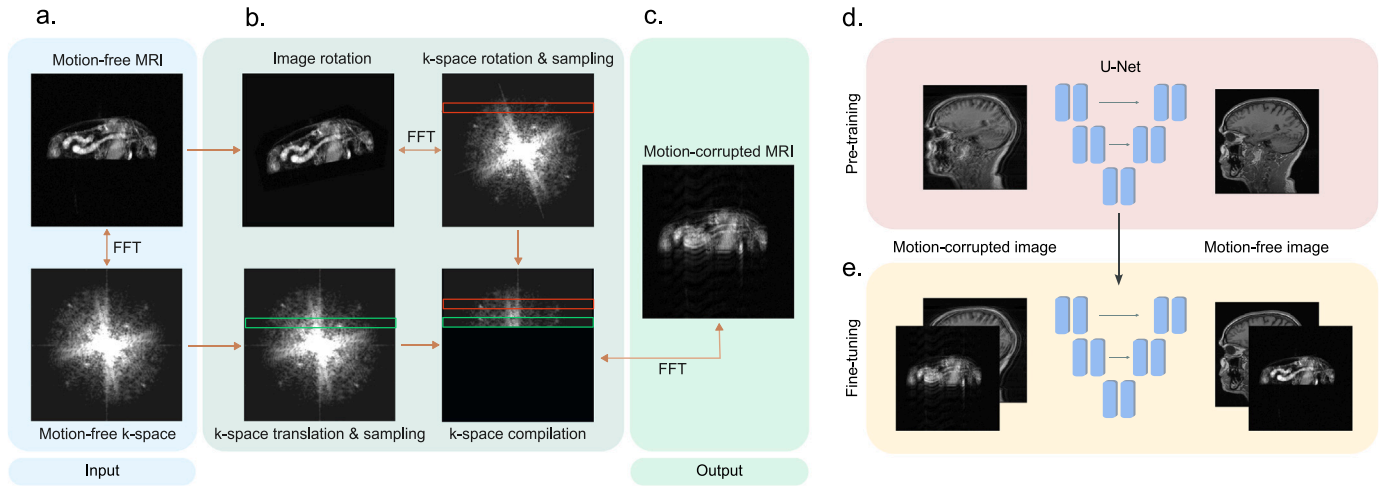
Fig. 4. Schematic diagram showing motion artifact simulation and the deep learning training pipeline. **(a)** Motion-free MRI and k-space magnitude images. **(b)** k-space compilation based on image rotation and k-space translation. **(c)** Reconstructed MRI magnitude image showing motion artifacts. **(d)** Pre-training the U-Net model with the brain MRI dataset. **(e)** Fine-tuning the model with a mixed dataset of brain and insect MRI images.

motion-free MRI magnitude images [9,12,13]. This presents significant challenges, especially in the context of MRI for small invertebrate organisms. Simulating bulk rigid-body motion artifacts from motion-free k-space and image-space is an effective approach for generating training datasets, as commonly reported in the clinical MRI motion correction literature [9]. We assumed in-plane rigid body motion and single-coil sequential Cartesian k-space acquisition. Motion mostly happened between individual k-space line acquisitions, known as inter-view motion. Motion during the acquisition of individual k-space lines over the period of the echo time was assumed to be negligible. According to the Fourier shift theorem, bulk translation motion induces a phase shift in the corresponding k-space line and by the Fourier rotation theorem, subject rotation results in corresponding rotation of the k-space line itself. We utilized a k-space technique for the translation motion simulation and image-space technique for simulating the rotational motion, following the approach outlined in [18]. The simulation pipeline was implemented in MATLAB (Mathworks Inc.), for which a schematic representation is provided in Fig. 4. Fig. 4(a) represents the motion-free MRI magnitude image and the corresponding k-space magnitude. Fig. 4(b) shows the k-space compilation process, where the image was rotated to varying degrees and the corresponding k-space was sampled, and similarly, the motion-free k-space was translated with varying amount and sampled for a motion corrupted k-space. Standard Cartesian Fourier reconstruction of this compiled k-space gives the motion-corrupted MR image, shown in Fig. 4(c). Although the schematic diagram shows the rotation and translation applied simultaneously for easier representation, independent translation and rotations of the images are feasible and effective for model training.

The original brain MRI dataset [17] comprised of 25 subjects, each with $256 \times 256 \times 170$ slices. To simulate motion artifacts, slices 11 to 160 were selected from each subject, resulting in a total of 3750 image pairs. Out of these, 3,000 image pairs were selected for the training set, and 400 image pairs were selected for the validation set. Translation motion artifacts were simulated by applying pseudo-random motion magnitudes within the normalized range $[-1, 1]$, scaled by three distinct motion severity levels (1, 2, 3), to phase encode lines [20:120, 145:220] of the 256 total phase encoding lines. This resulted in spatial domain translations ranging from 1 to 10 pixels in both the X and Y directions. A separate rotational motion dataset was generated using the first 10 subjects out of the same 25 subjects, yielding 1500 image pairs, which were divided into 1400 training and 100 validation sets. Rotation magnitudes were pseudo randomly selected between -1 and 1 pixel degrees applied to phase encoding lines [80:120, 150:220]

of the 256 lines. Final training set and validation set for the pre-training of the model resulted in 4400 and 500 image pairs respectively. The motion artifact simulation of the small insect dataset followed the same pipeline, resulting in a training dataset of 500 image pairs and a validation dataset of 55 image pairs. Further details on the motion artifact simulation can be found in the supplementary information.

2.4.3. Deep learning model architecture and training

We followed a transfer learning approach for model training, with the larger brain MRI dataset used for pre-training the model (as represented in Fig. 4(d)), and the smaller insect MRI dataset used for end-to-end fine-tuning of the model, as represented in Fig. 4(e). To mitigate catastrophic forgetting, we fine-tuned the model using a mixed dataset composed of a subset of the pre-training and insect MRI dataset in a 50:50 ratio. Our model was based on a modified version of the standard U-Net architecture [19] originally developed for biomedical image segmentation, featuring an encoder–decoder architecture with skip connections for capturing local and global features. The encoder part of the model consisted of five hierarchical levels with feature channels [16,32,64,128,256], and a single-channel input size of 256×256 was used as the initial layer. Each level of the encoder used one DoubleConv block with two 3×3 convolutional layers, each followed by batch normalization and ReLU activation. 2×2 max-pooling was used for downsampling to reduce spatial dimensions and increasing the feature channels. The bottleneck part consisted of two convolutional layers with 512 feature channels for extracting high-level features. The decoder part performed upsampling by 2×2 transposed convolutions with stride 2. DoubleConv layers followed the upsampling for feature refinement, and the skip connections from the corresponding encoder layers to retain spatial details. The final layer was a 1×1 convolutional layer to map the output to a single-channel 256×256 size motion-corrected MR magnitude image.

For pre-training the model, we used the brain MRI dataset consisting of simulated motion-corrupted and motion-free image pairs with a 4400-500 training-validation split. Image preprocessing and augmentation included intensity normalization, rotation, horizontal and vertical flipping to enhance the model's robustness. We trained the model using a Mean Squared Error (MSE) loss function as a pixel-wise image-to-image regression task, with a mini-batch size of 12. The Adam optimizer [20] with an initial learning rate of 0.0001 was used, employing early stopping if validation loss did not improve for 20 epochs with a delta of 0.0001. The learning rate was reduced to 0.00001 when the validation loss plateaued at the final epoch of 72. All the model parameters were determined empirically through experimentation.
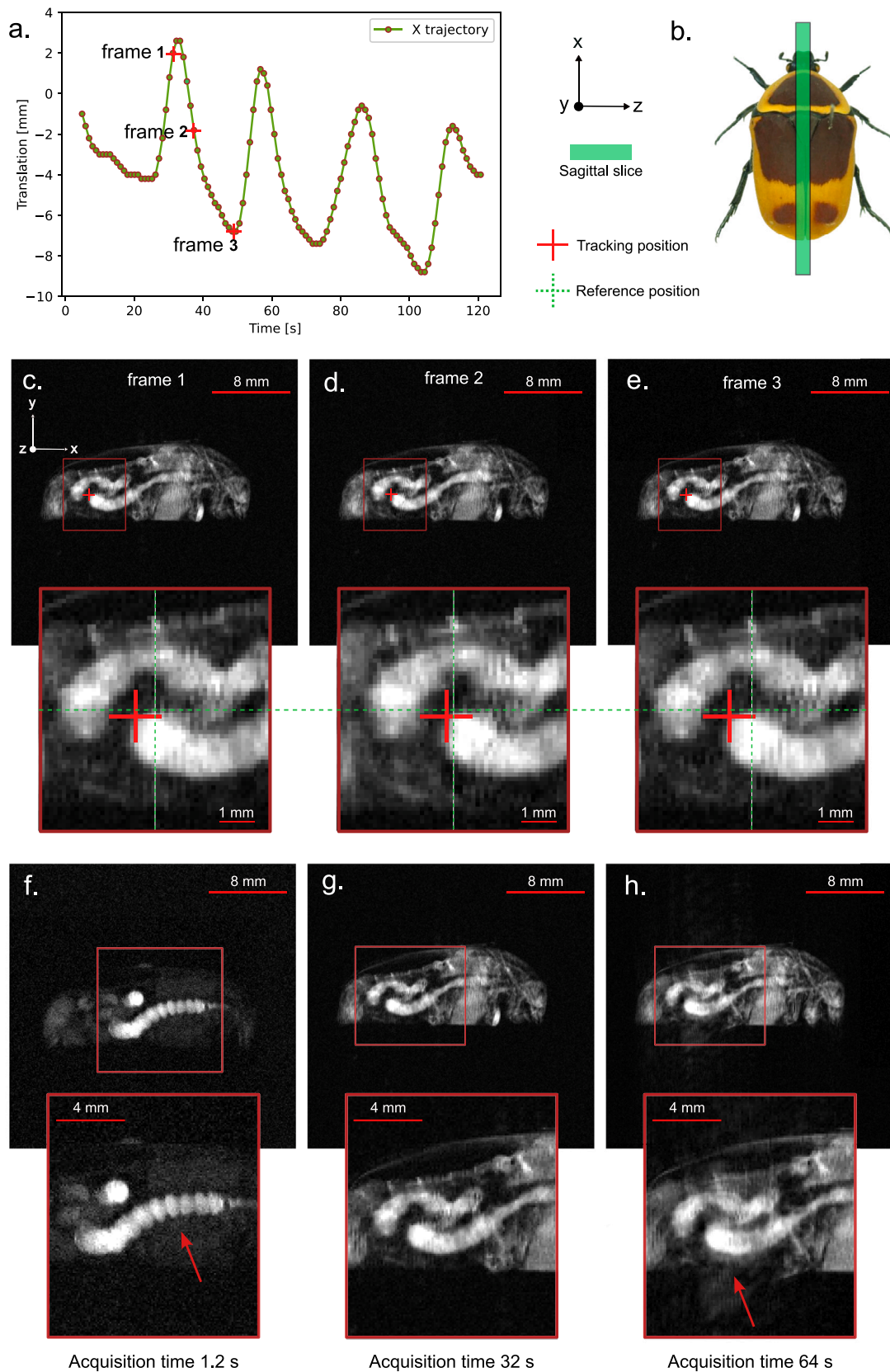
Fig. 5. Internal organ motion of a dormant insect. **(a)** Motion trajectory of the marked keypoint on the insect's digestive system estimated using an algorithm based on optical flow. **(b)** MRI sagittal slice reference position. **(c)** Internal organ motion, phase 1. **(d)** Internal organ motion, phase 2. **(e)** Internal organ motion, phase 3. **(f)** Single frame acquisition time of $1.2\,s$, revealing the corrugated structure of the midgut and almost no motion artifact. **(g)** Single frame acquisition time of 32 s resulting in medium level motion artifacts. **(h)** Single frame acquisition time of 64 s shows larger motion artifacts.
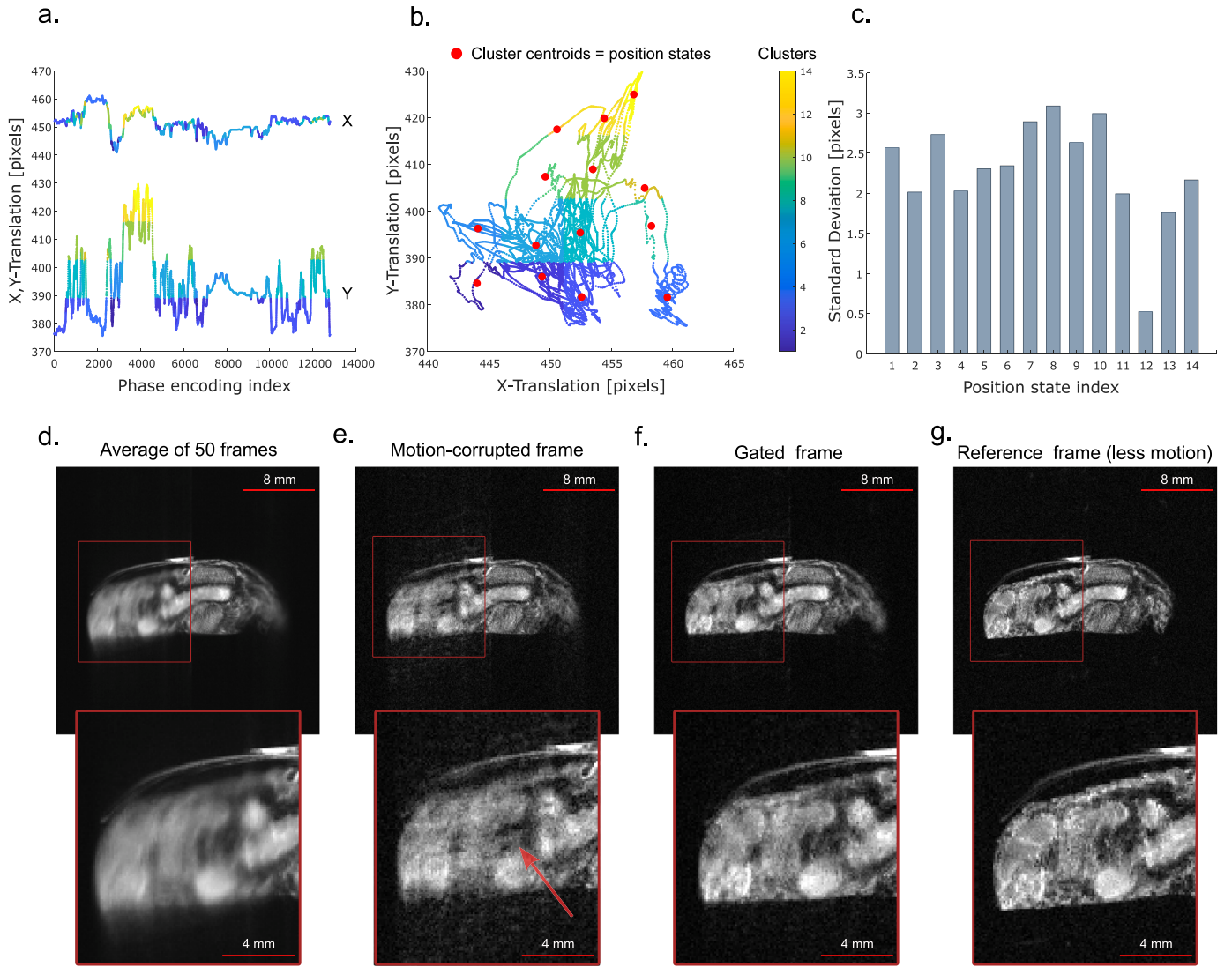
Fig. 6. Retrospective gating for motion compensated MRI. **(a)** X&Y-motion trajectory of the selected keypoint for the duration of MRI raw data acquisition, color-coding represents the different spatial clusters. **(b)** 2D X-Y plot of the same motion trajectory, with color-coding represents the grid-based clusters with the centroid defines the different position states for gating. **(c)** Standard deviation of distance from the centroid of the individual clusters. **(d)** Average magnitude image of 50 MRI frames showing the extend of motion-artifacts. **(e)** Sample motion-corrupted frame out of the reconstructed 50 frames without motion compensation. **(f)** Retrospectively gated MRI frame showing reduction in motion-artifacts. **(g)** Reference image with less motion artifacts.

For fine-tuning the model, we used a mixed dataset consisting of 500 brain (a subset of the pre-training dataset) and 500 insect MR image pairs for the training set, and validation set of 80 image pairs (25 brain and 55 insect MRI). The end-to-end fine-tuning was performed with all training parameters remaining the same as those used in pre-training, except that the training was limited to 30 epochs to prevent overfitting. Additionally, we used a combined MSE-SSIM loss (0.2:0.8), empirically weighted to optimize both pixel-level accuracy and perceptual quality for the small insect dataset. The performance of the model was evaluated using both simulated motion-corrupted images and real experimental motion-corrupted images, presented in the following sections. All deep learning experiments were carried out on a workstation equipped with an NVIDIA RTX A5000 GPU, having 24 GB of dedicated memory with CUDA support, and 256 GB of RAM. The development environment comprised of the Spyder 5.4.3 IDE, Python 3.9.17, the PyTorch [21] library running on the Windows 10 (Microsoft, 2019) operating system. Further details on the deep learning problem formulation and architecture can be found in the supplementary information.

2.5. Image quality metrics

We used two image quality metrics for the quantitative assessment of improvement in the image quality after the residual motion correction. The Structural Similarity Index Measure (SSIM) [22] was employed to evaluate the perceived quality of the corrected images. It is a full-reference metric, which assesses image similarity by analyzing luminance, contrast, and structural details. It calculates a score between −1 and 1, where 1 indicates perfect similarity, 0 indicates no similarity, and −1 indicates perfect dissimilarity. This measure is known to correlate well with human visual perception. We also used the gradient entropy (GE) as a reference-free image quality metric, especially for evaluating motion correction in real experimental data, where an absolute motion-free reference image was unavailable. GE provides a measure of the randomness of image gradient magnitudes expressing the richness of the edge information. This can be calculated by computing the histogram entropy of the normalized image gradient magnitudes. In the context of MRI motion correction, lower gradient entropy values generally indicate more structured and well-defined edges, which correspond to higher image quality [23,24]. SSIM and

GE were calculated using custom Python scripts (OpenCV [25] v4.10.0, scikit-image [26] v0.21.0, SciPy [27] v1.11.1). Further details can be found in the supplementary information.

2.6. Animal handling and ethical statement

We used live adult specimens of *Pachnoda marginata* beetles for the insect MRI experiments, which were obtained from an online pet store (https://thepetfactory.de). A custom-made terrarium was used to keep the beetles at room temperature, with water and fruits provided according to the vendor's recommendations. For retrospective gating dynamic MRI imaging studies of the behaving insect, we tethered the insect using a UV-curable adhesive. The beetle was initially immobilized by cooling for 15 min, then placed in a ventilated container. A drop of adhesive was applied to a 3D-printed PLA tether and positioned near the scutellum on the dorsal side of the insect. The adhesive was cured under a UV lamp for 10 s, and then the tethered insect on the treadmill was positioned inside an RF volume coil for the MRI experiments. For the deep learning training dataset generation, the same protocols was followed with longer cooling time of around 30 min, to generate motion-free images, and the inactivity of the beetle was monitored and validated with the *in situ* computer vision system. After the experiments, the tether was removed using a cotton swab soaked in warm water. The insects were euthanized following the study.

3. Results

3.1. MRI of the dormant insect: Internal organ motion

To capture internal organ dynamics in the dormant insect, high-resolution sagittal-plane images were acquired using the RARE sequence with a repetition time of $500\,\text{ms}$, echo time of $5\,\text{ms}$, image size of 256×256 pixels with a FOV of $30\,\text{mm} \times 30\,\text{mm}$, resulting in an in-plane resolution of $117\,\mu\text{m} \times 117\,\mu\text{m}$, slice thickness of $3\,\text{mm}$, no signal average, RARE factor of four, 20 repetitions, for the dynamic MRI frames, and a total acquisition time of $640\,\text{s}$. The motion trajectory of the selected keypoint on the digestive system is also shown in Fig. 5(a), confirming the periodic internal organ motion; the corresponding video file (Video 2) is provided in the supplementary information.

Although each frame required an acquisition time of $32\,\text{s}$ for this particular MRI experiment, the dormant state of the insect featured slow internal organ motion, making the reconstruction less prone to motion artifacts. But this is not the case for an active insect and will have more blurring, as shown in Fig. 2(l)&(m). The various internal motions of the insect had different time scales and the sharpness of the resulting MRI reconstruction depended on the acquisition speed of the imaging sequence. Fig. 5(h) shows the same sagittal slice and was based on identical MRI parameters, except for a TR of $1000\,\text{ms}$ and RARE factor of 4, resulting in an effective acquisition time of $64\,\text{s}$ per frame. Here, the zoomed-in image clearly shows motion artifacts caused by internal organ movement, which can be compared to Fig. 5(g), acquired over $32\,\text{s}$ for the same specimen and similar physiological state. This can be further validated with the following MRI of the same sagittal section, based on much faster acquisition. The same sequence with much shorter TR of $75\,\text{ms}$, RARE factor of 10, and a partial Fourier acquisition of 160 k-space lines with homodyne reconstruction (Paravision 360v3.3) resulted in an effective acquisition time of $1.2\,\text{s}$ per frame. This relatively fast acquisition shows the corrugated structure of the insect midgut displayed in Fig. 5(f), which normally involves peristaltic wave propagation throughout the structure. For slower acquisitions as discussed earlier, the peristaltic motion renders the whole midgut as a single cylindrical structure without any corrugation. The experiment was designed solely to illustrate the impact of imaging timescale on motion sensitivity. The low signal intensity observed in the MR images is attributed to the short repetition time (TR), which limits longitudinal magnetization recovery between excitations and consequently reduces overall signal.

3.2. Retrospective gating for non-rigid motion correction

Retrospective gating was performed using the developed Algorithm 1. Fig. 6(d) shows the average of the 50 MRI magnitude images, highlighting the extent of motion artifacts. An example of a motion-corrupted MRI frame from this set is shown in Fig. 6(e). Initial motion compensation achieved through gated reconstruction is illustrated in Fig. 6(f). For reference, Fig. 6(g) presents an MRI frame of the same slice without the large-scale abdominal motion. Fig. 3(b) visualizes the multi-rigid abdominal position states of the insect as it behaves on the treadmill. While the current proof-of-concept experiment presents a single gated MRI frame reconstruction corresponding to a single position state, the approach allows for reconstruction of multiple frames, depending on the motion dynamics of the behaving insect.

3.3. Deep learning residual motion correction

3.3.1. Motion correction on simulated test data

The deep learning model fine-tuned with the small insect dataset was used for correcting simulated motion artifacts of a test dataset generated from 100 insect MRI images. Fig. 7(a) shows a sample motion-corrupted image from the dataset. The motion-corrected image using the model is shown in Fig. 7(b), and the corresponding ground truth motion-free image is shown in Fig. 7(c) for comparison. Fig. 7(d) shows the histogram plot of the calculated structural similarity index measure (SSIM) values for the test dataset before and after correction, with corresponding SSIM $mean \pm S.D$ of 0.668 ± 0.080 and 0.847 ± 0.055, showing significant reduction in the motion artifacts. The effectiveness of the correction was further validated using the gradient entropy (GE) measure. The GE histogram for the same test dataset (Fig. 7(e)) showed a significant reduction in the $mean \pm S.D$, from 2.985 ± 0.190 before correction to 2.231 ± 0.143 after correction.

3.3.2. Motion correction on experimental test data

The performance of the same fine tuned model mentioned in Section 3.3.1 was evaluated on real experimental MRI motion-corrupted data. Fig. 8(a) shows the retrospectively gated MR image frame as initial motion compensation described in Section 3.2, with the corresponding gradient entropy value of 3.154. The reconstructed image shows residual motion artifacts, which were addressed using the deep learning correction method described in Section 2.4. The motion corrected image is shown in Fig. 8(b), with the gradient entropy value reduced to 2.381, showing evident reduction in the motion artifacts.

Motion artifact severity directly correlated with the activity of the insect during the MR k-space acquisition. Initial motion compensation by retrospectively gated MRI reconstruction was only needed for the severe case of multi-rigid motion, with relatively large scale translation of the abdomen as mentioned in Section 2.3. A less severe motion-corrupted image as shown in Fig. 8(c) could be directly corrected using the same deep learning model, which is shown in Fig. 8(d). The gradient entropy value was reduced from 3.280 to 2.143, showing visible reduction in motion artifacts in this case. Fig. 8(e) presents the bar graph of gradient entropy values before and after deep learning correction, for both gated and non-gated MRI reconstruction.

4. Discussion and conclusion

Technological advancements in high-field magnetic resonance are opening up the possibility of non-invasive *in-vivo* studies of behaving model organisms. The advent of ultra-high-field MRI systems significantly enhances the acquisition signal-to-noise ratio (SNR), paving the way for dynamic imaging studies. However, method developments for accommodating these experiments appear to face inherent limitations due to subject motion, a persistent challenge in MRI since its inception. This is further exacerbated by the inherently complex nature of loco-motion in non-invertebrate model organisms. Internal organ motion
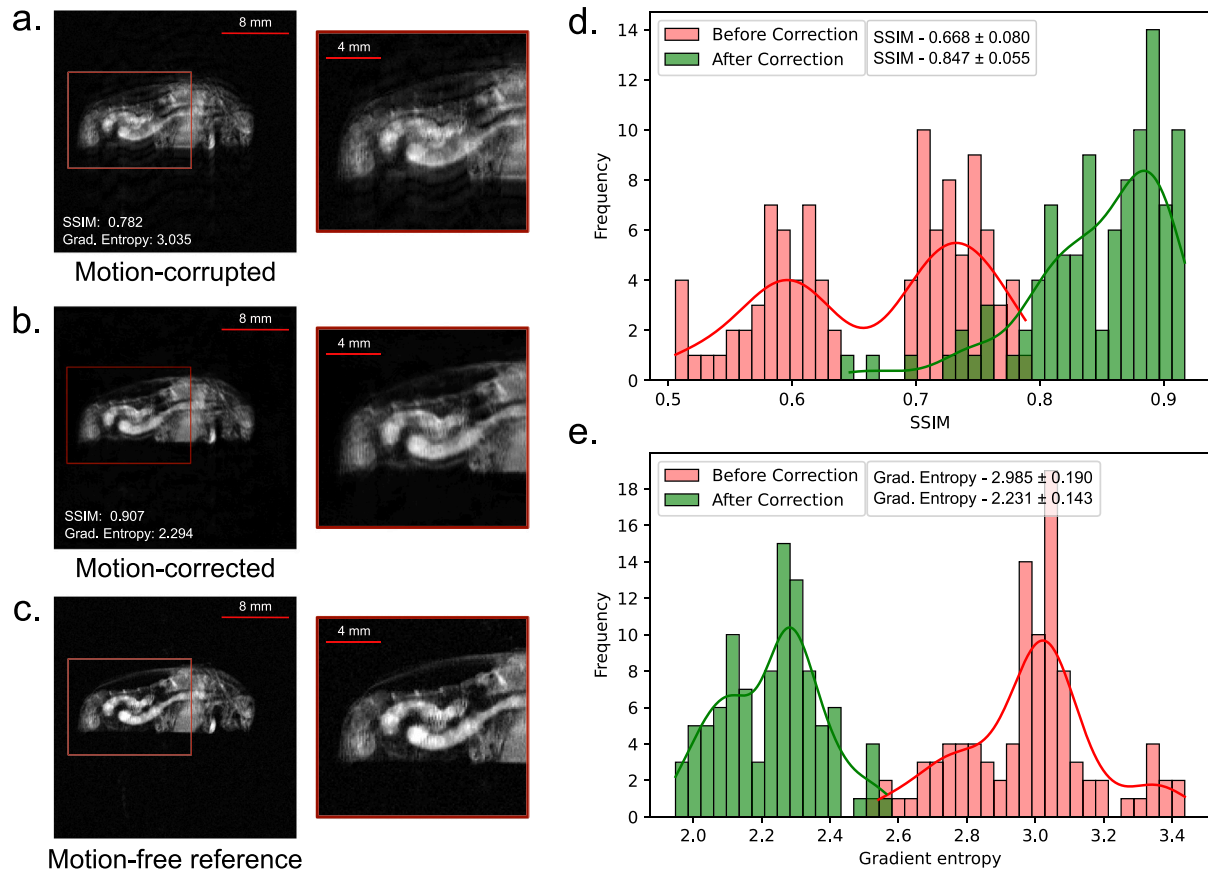
Fig. 7. Deep learning motion correction on a simulated dataset. **(a)** Simulated motion-corrupted test image. **(b)** Motion-corrected image with the fine-tuned model. **(c)** Motion-free reference for comparison. **(d)** SSIM histogram of test images before and after correction. **(e)** Gradient entropy histogram of test images before and after correction.
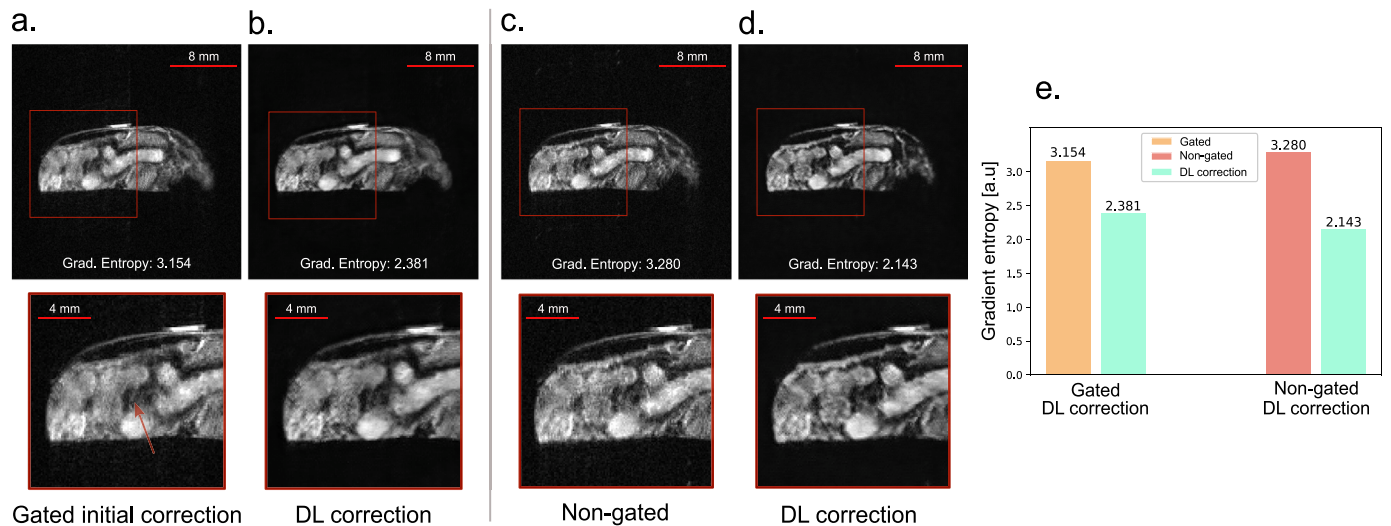

Fig. 8. Deep learning motion correction on experimental dataset. **(a)** Retrospectively gated image with residual motion artifacts. **(b)** Deep learning motion-corrected image. **(c)** Non-gated image with less severe motion artifacts. **(d)** Deep learning based motion-corrected image. **(e)** Gradient entropy value before and after deep learning motion correction.

is another substantial source of motion artifacts, depending on the MR imaging time scale. This is mainly due to the combined effect of the circulatory system which pumps the hemolymph through the body cavity, the peristaltic digestive movements to transport food from the mouth through the esophagus, crop, midgut, hindgut, and eventually exiting the body, and tracheal compression for respiration. Although

the overall effect of these movements manifested as blurring and ghosting artifacts in MRI under normal imaging sequence settings, faster MRI techniques can reduce these artifacts and enable visualization of different motion states. In the present study, the sagittal MRI slice (position shown in Fig. 5(b)) of the inactive insect on the treadmill, acquired using a relatively slower MRI sequence reveals distinct phases

of digestive system peristalsis, as illustrated in the T1-weighted frames 1–3 (Figs. 5(c)–(e)). This was made possible by the dormancy of the insect.

Motion parameter estimation and quantification using external hardware has been widely used in both prospective as well as retrospective motion correction strategies [14,28–30]. While relatively straightforward for global rigid body motion, analytically modeling retrospective motion correction using estimated motion parameters becomes significantly more challenging when addressing non-rigid kinematics. In the case of insect abdominal motion during tethered locomotion, the dynamics could be approximated as semi-periodic multi-rigid motion, allowing the use of gating-based methods for the initial motion-compensated MRI reconstruction. Subsequently, a deep learning correction method could address residual motion artifacts, primarily caused by rigid body motion components. The overall method or correction pipeline developed here is not a general solution to all the complex dynamics of a behaving organism's movement during MRI. However, in principle, an end-to-end deep learning model can be trained to address the complex non-rigid nature of behavioral dynamics of a model organism. But this greatly depends on the successful modeling of the particular insect's locomotion, and the subsequent faithful MRI motion artifact simulation for generating the training dataset.

There are various approaches to implementing deep learning MRI motion correction, with many studies concentrating on a rigid body motion approximation to model motion artifacts. These methods have demonstrated significant improvements in motion compensation over traditional techniques [9]. Due to the limited availability of motion-corrupted insect MRI datasets, we utilized a transfer learning approach for training the model. Transfer learning provides an effective solution to overcoming data scarcity challenges in various clinical MRI research applications [31,32]. A pre-trained model is fine-tuned on a smaller, specialized dataset, utilizing the knowledge and features acquired during its initial training. It demonstrated robust performance by effectively capturing shared motion patterns and artifact characteristics across brain and insect MRI, despite notable anatomical differences. Although our MRI fine-tuning dataset focused on a single insect species, this method has the potential to be adapted for multiple species, providing a robust and generalized solution for addressing motion artifacts in MRI studies of behaving invertebrate model organisms.

CRediT authorship contribution statement

Ajmal Chenakkara: Writing – original draft, Visualization, Validation, Software, Methodology, Investigation, Formal analysis. **Mazin Jouda:** Writing – review & editing, Supervision, Investigation, Conceptualization. **Ulrike Wallrabe:** Writing – review & editing, Supervision, Conceptualization. **Jan G. Korvink:** Writing – review & editing, Supervision, Resources, Project administration, Funding acquisition, Conceptualization.

Acknowledgments

Funding

Declaration of competing interest

The authors declare the following financial interests/personal relationships which may be considered as potential competing interests: Jan G. Korvink reports a relationship with Voxalytic GmbH that includes: board membership and equity or stocks. Ulrike Wallrabe reports a relationship with Voxalytic GmbH that includes: board membership and equity or stocks. If there are other authors, they declare that they have no known competing financial interests or personal relationships that could have appeared to influence the work reported in this paper.

Appendix A. Supplementary data

Supplementary material related to this article can be found online at https://doi.org/10.1016/j.jmr.2025.107954.

Data availability

The code and datasets used in this study are publicly available at: https://github.com/chenakkara/Treadmill_MRI_residual_motion_correction.git.

References

[1] J. Maclaren, M. Herbst, O. Speck, M. Zaitsev, Prospective motion correction in brain imaging: A review, Magn. Reson. Med. 69 (3) (2013) 621–636, http://dx.doi.org/10.1002/mrm.24314.

[2] F. Godenschweger, U. Kägebein, D. Stucht, U. Yarach, A. Sciarra, R. Yakupov, F. Lüsebrink, P. Schulze, O. Speck, Motion correction in MRI of the brain, Phys. Med. Biology 61 (5) (2016) http://dx.doi.org/10.1088/0031-9155/61/5/R32.

[3] A. Chenakkara, M. Jouda, U. Wallrabe, J.G. Korvink, Treadmill MRI enables noninvasive tracking of Pachnoda marginata biomechanics, 2025, submitted for publication.

[4] V. Runge, J. Clanton, C. Partain, A. James Jr., Respiratory gating in magnetic resonance imaging at 0.5 Tesla., Radiology 151 (2) (1984) 521–523.

[5] R.L. Ehman, M. McNamara, M. Pallack, H. Hricak, C. Higgins, Magnetic resonance imaging with respiratory gating: techniques and advantages, Am. J. Roentgenol. 143 (6) (1984) 1175–1182.

[6] P. Lanzer, C. Barta, E. Botvinick, H. Wiesendanger, G. Modin, C. Higgins, ECG-synchronized cardiac MR imaging: method and evaluation., Radiology 155 (3) (1985) 681–686.

[7] J. Maclaren, O. Speck, D. Stucht, P. Schulze, J. Hennig, M. Zaitsev, Navigator accuracy requirements for prospective motion correction, Magn. Reson. Med.: An Off. J. the Int. Soc. Magn. Reson. Med. 63 (1) (2010) 162–170.

[8] B. Zahneisen, B. Keating, T. Ernst, Propagation of calibration errors in prospective motion correction using external tracking, Magn. Reson. Med. 72 (2) (2014) 381–388.

[9] V. Spieker, H. Eichhorn, K. Hammernik, D. Rueckert, C. Preibisch, D.C. Karampinos, J.A. Schnabel, Deep learning for retrospective motion correction in MRI: a comprehensive review, IEEE Trans. Med. Imaging (2023).

[10] Y. Chang, Z. Li, G. Saju, H. Mao, T. Liu, Deep learning-based rigid motion correction for magnetic resonance imaging: a survey, Meta-Radiology (2023) 100001.

[11] Z. Chen, K. Pawar, M. Ekanayake, C. Pain, S. Zhong, G.F. Egan, Deep learning for image enhancement and correction in magnetic resonance imaging—state-of-the-art and challenges, J. Digit. Imaging 36 (1) (2023) 204–230.

[12] P.M. Johnson, M. Drangova, Conditional generative adversarial network for 3D rigid-body motion correction in MRI, Magn. Reson. Med. 82 (3) (2019) 901–910, http://dx.doi.org/10.1002/MRM.27772.

[13] T. Küstner, K. Armanious, J. Yang, B. Yang, F. Schick, S. Gatidis, Retrospective correction of motion-affected MR images using deep learning frameworks, Magn. Reson. Med. 82 (4) (2019) 1527–1540.

[14] M. Zaitsev, C. Dold, G. Sakas, J. Hennig, O. Speck, Magnetic resonance imaging of freely moving objects: prospective real-time motion correction using an external optical motion tracking system, NeuroImage 31 (3) (2006) 1038–1050, http://dx.doi.org/10.1016/J.NEUROIMAGE.2006.01.039, URL https://www.sciencedirect.com/science/article/pii/S1053811906000917?via%3Dihub.

[15] J. Yosinski, J. Clune, Y. Bengio, H. Lipson, How transferable are features in deep neural networks? Adv. Neural Inf. Process. Syst. 27 (2014).

[16] J. Donahue, Y. Jia, O. Vinyals, J. Hoffman, N. Zhang, E. Tzeng, T. Darrell, Decaf: A deep convolutional activation feature for generic visual recognition, in: International Conference on Machine Learning, PMLR, 2014, pp. 647–655.

[17] R. Souza, O. Lucena, J. Garrafa, D. Gobbi, M. Saluzzi, S. Appenzeller, L. Rittner, R. Frayne, R. Lotufo, An open, multi-vendor, multi-field-strength brain MR dataset and analysis of publicly available skull stripping methods agreement, NeuroImage 170 (2018) 482–494.

[18] M.A. Al-masni, S. Lee, J. Yi, S. Kim, S.M. Gho, Y.H. Choi, D.H. Kim, Stacked U-Nets with self-assisted priors towards robust correction of rigid motion artifact in brain MRI, NeuroImage 259 (March) (2022) 119411, http://dx.doi.org/10.1016/j.neuroimage.2022.119411.

[19] O. Ronneberger, P. Fischer, T. Brox, U-net: Convolutional networks for biomedical image segmentation, in: International Conference on Medical Image Computing and Computer-Assisted Intervention, Springer, 2015, pp. 234–241.

[20] D.P. Kingma, J. Ba, Adam: A method for stochastic optimization, 2014, arXiv preprint arXiv:1412.6980.

[21] A. Paszke, S. Gross, F. Massa, A. Lerer, J. Bradbury, G. Chanan, T. Killeen, Z. Lin, N. Gimelshein, L. Antiga, et al., Pytorch: An imperative style, high-performance deep learning library, Adv. Neural Inf. Process. Syst. 32 (2019).

[22] Z. Wang, A.C. Bovik, H.R. Sheikh, E.P. Simoncelli, Image quality assessment: from error visibility to structural similarity, IEEE Trans. Image Process. 13 (4) (2004) 600–612.

[23] E. Marchetto, H. Eichhorn, D. Gallichan, J.A. Schnabel, M. Ganz, Agreement of image quality metrics with radiological evaluation in the presence of motion artifacts, 2024, arXiv preprint arXiv:2412.18389.

[24] K.P. McGee, A. Manduca, J.P. Felmlee, S.J. Riederer, R.L. Ehman, Image metric-based correction (autocorrection) of motion effects: analysis of image metrics, J. Magn. Reson. Imaging: An Off. J. the Int. Soc. Magn. Reson. Med. 11 (2) (2000) 174–181.

[25] G. Bradski, The OpenCV library, Dr. Dobb's J. Softw. Tools (2000).

[26] S. Van der Walt, J.L. Schönberger, J. Nunez-Iglesias, F. Boulogne, J.D. Warner, N. Yager, E. Gouillart, T. Yu, scikit-image: image processing in Python, PeerJ 2 (2014) e453.

[27] P. Virtanen, R. Gommers, T.E. Oliphant, M. Haberland, T. Reddy, D. Cournapeau, E. Burovski, P. Peterson, W. Weckesser, J. Bright, et al., SciPy 1.0: fundamental algorithms for scientific computing in Python, Nat. Methods 17 (3) (2020) 261–272.

[28] M. Zaitsev, J. Maclaren, M. Herbst, Motion artifacts in MRI: A complex problem with many partial solutions, J. Magn. Reson. Imaging 42 (4) (2015) 887–901, http://dx.doi.org/10.1002/jmri.24850.

[29] O. Speck, J. Hennig, M. Zaitsev, Prospective real-time slice-by-slice motion correction for fMRI in freely moving subjects, Magn. Reson. Mater. Phys. Biology Med. 19 (2006) 55–61.

[30] P. DiGiacomo, J. Maclaren, M. Aksoy, E. Tong, M. Carlson, B. Lanzman, S. Hashmi, R. Watkins, J. Rosenberg, B. Burns, et al., A within-coil optical prospective motion-correction system for brain imaging at 7T, Magn. Reson. Med. 84 (3) (2020) 1661–1671.

[31] R.S. Pemmasani Prabakaran, S.W. Park, J.H. Lai, K. Wang, J. Xu, Z. Chen, A.-m.O. Ilyas, H. Liu, J. Huang, K.W. Chan, Deep-learning-based super-resolution for accelerating chemical exchange saturation transfer MRI, NMR Biomed. (2024) e5130.

[32] S.U.H. Dar, M. Özbey, A.B. Çatlı, T. Çukur, A transfer-learning approach for accelerated MRI using deep neural networks, Magn. Reson. Med. 84 (2) (2020) 663–685.